

Experimental study of exospheric hydrogen atom distributions by Lyman-alpha detectors on the TWINS mission

J. Bailey¹ and M. Gruntman¹

Received 8 February 2011; revised 11 May 2011; accepted 7 June 2011; published 7 September 2011.

[1] Exospheric atomic hydrogen (H) resonantly scatters solar Lyman- α (121.567 nm) radiation, observed as the geocorona. Measurements of scattered solar photons allow one to probe time-varying three-dimensional distributions of exospheric H atoms. The Two Wide-angle Imaging Neutral-atom Spectrometers (TWINS) mission images the magnetosphere in energetic neutral atom (ENA) fluxes and additionally carries Lyman- α detectors (LADs) to investigate exospheric atomic hydrogen. Knowledge of exospheric properties is essential for the interpretation of magnetospheric images in ENA fluxes produced in charge exchange between energetic ions and H atoms. We describe the process of obtaining exospheric distributions and present, as an example, a global H number density distribution for 11 June 2008. The TWINS LAD experimental data are especially sensitive to atomic hydrogen at geocentric distances from 3 to 8 Earth radii. The distribution reveals asymmetries from day to night, dawn to dusk, and north to south. We discuss the available data sets and their coverage, limitations, and promise for a study of exospheric response to seasonal, solar, and geomagnetic variations.

Citation: Bailey, J., and M. Gruntman (2011), Experimental study of exospheric hydrogen atom distributions by Lyman-alpha detectors on the TWINS mission, *J. Geophys. Res.*, 116, A09302, doi:10.1029/2011JA016531.

1. Exosphere

[2] The most abundant neutral constituent in Earth's upper exosphere, atomic hydrogen (H), resonantly scatters solar Lyman- α (121.567 nm) radiation — creating a phenomenon known as the geocorona. Space-based measurements of the geocorona allow reconstruction of the global H distribution over time scales which depend on observational coverage. We use such measurements, from detectors on a pair of satellites in widely spaced highly elliptical Molniya-type orbits, to obtain exospheric spatial distributions on a daily basis.

[3] The geocorona reveals an exosphere that is asymmetric, including higher nightside densities, sometimes called the geotail [e.g., *Thomas and Bohlin*, 1972; *Bertaux and Blamont*, 1973; *Carruthers et al.*, 1976; *Rairden et al.*, 1986; *Østgaard et al.*, 2003; *Zoennchen et al.*, 2010]. In this article, we focus on geocentric distances $r > 3 R_E$ ($1 R_E = 6371$ km is Earth's mean radius), where the H densities are low enough to assume optically thin conditions. In this single scattering environment, the observed intensity of scattered Lyman- α radiation is simply proportional to the integral of the H density over the line of sight. As discussed in section 4.2, the uncertainty introduced by this assumption does not exceed 20% at the

minimal geocentric distance of $3 R_E$ and decreases with altitude. Closer to Earth, the denser conditions require a much more complex essentially radiation transfer treatment [e.g., *Thomas*, 1963; *Meier*, 1969; *Meier and Mange*, 1970; *Anderson and Hord*, 1977; *Rairden et al.*, 1986; *Bush and Chakrabarti*, 1995; *Bishop*, 1999] that is beyond the scope of this work.

[4] As initially described by *Chamberlain* [1963], the exosphere comprises three main particle populations, ballistic, escaping, and satellite, moving in Earth's gravitational field and influenced by solar radiation pressure. Atoms in ballistic trajectories rise from the exobase, which is usually assumed to be between 400 and 800 km, depending on solar conditions, and eventually fall back. Atoms with velocities larger than escape velocities depart from the exobase and leave on hyperbolic trajectories. Atoms in satellite trajectories have been scattered or injected into closed orbits by rare elastic collisions or charge exchange, respectively, and do not intersect the exobase.

[5] Ballistic trajectories dominate in a region immediately above the exobase. As the density of this population rapidly decreases toward higher altitudes, satellite particles begin to dominate above where some of the collisions and subsequent orbit apses occur. Escaping particles are present at all altitudes and at higher altitudes they are the only terrestrial population that remains. Farther away from Earth, extraterrestrial hydrogen becomes dominant. This interplanetary population principally comprises inflowing interstellar H atoms from the local interstellar medium (LISM) [e.g., *Fahr*, 1974; *Holzer*, 1977; *Meier*, 1977; *Thomas*, 1978; *Bertaux*, 1984; *Clarke et al.*, 1998; *Stephan et al.*, 2001; *Quémerais et al.*, 2003]. It

¹Department of Astronautical Engineering, Viterbi School of Engineering, University of Southern California, Los Angeles, California, USA.

is also possible that energetic neutral atoms (ENAs) originating in the heliospheric sheath region contribute significantly to neutral atoms within 1 AU from the Sun [Gruntman and Izmodenov, 2004; Schwadron and McComas, 2010]. At 1 AU, the extraterrestrial H number density varies between 10^{-4} and 10^{-2} cm^{-3} .

[6] Solar radiative heating largely determines temperature and density at the exobase, which, in turn, causes a departure from spherical symmetry of the exosphere. Heating of the upper atmosphere on the dayside, by solar X-ray and extreme ultraviolet (EUV) radiation, also causes asymmetry. For example, a seasonal north-south asymmetry occurs as solar illumination differs between the summer and winter polar regions. In addition, a coupling effect via charge exchange exists between the exosphere and plasmasphere [e.g., Bishop, 1985; Rairden et al., 1986; Tinsley et al., 1986; Hodges, 1994].

[7] Beyond a few Earth radii, the Keplerian motion of H atoms is also highly susceptible to an effective pressure caused by solar Lyman- α radiation. This radiation pressure force varied between the extremes of 0.85 and 2.1 times the Sun's gravitational attraction of H atoms over the last five solar cycles. The effect of this radiation pressure is rather complex and the details of how it influences the satellite population is not quantitatively completely understood yet. Some argue that the satellite population would extend in the antisolar direction, contributing to the geotail [Bertaux and Blamont, 1973; Bertaux et al., 1995; Østgaard et al., 2003; Zoennchen et al., 2010]. However, this intuitive explanation contradicts the theoretical predictions made by Chamberlain [1979] and Hodges [1994] who suggested that the geotail was not enhanced as a result of solar radiation pressure rotating the line of apsides of satellite H orbits such that the apogees are shifted away from the Sun.

[8] Several space experiments have observed the geocorona under various conditions. The first geocoronal Lyman- α measurements were obtained by sounding rocket experiments that started in the late 1950s [e.g., Kupperian et al., 1959; Donahue, 1966]. In comparison to rocket-born experiments, satellite missions provided observations over longer time scales. In particular, these longer duration observations were first recorded by four of the Orbiting Geophysical Observatory satellites, OGO-3, -4, -5, and -6 [Bertaux and Blamont, 1970; Mange and Meier, 1970; Thomas, 1970]. Measurements by one of the Orbiting Solar Observatory satellites, OSO-4, were also used extensively to model the exosphere [Thomas and Bohlin, 1972; Bertaux and Blamont, 1973; Meier and Mange, 1973; Thomas and Anderson, 1976]. The interplanetary spacecraft Mariner 5 observed the dayside geocorona as it departed for Venus [Wallace et al., 1970]. Additionally, images of the geocorona were captured on the Apollo 16 mission [Carruthers et al., 1976].

[9] More recently, Rairden et al. [1983, 1986] fit a spherically symmetric model to geocoronal measurements by Dynamics Explorer 1 (DE 1). They also experimentally confirmed the existence of a geotail.

[10] Hodges [1994] used Monte Carlo simulations to obtain asymmetric global H distributions under solar conditions characterized by F10.7 values representative of a typical solar cycle. For each used F10.7 value (80, 130, 180, and 230), distributions were presented for both equinox and solstice. The H concentrations were noticeably greater at

solstice. In addition, his theoretical predictions exhibited an enhancement in the antisolar direction (geotail) and a secondary enhancement in the solar direction. By running simulations with and without resonant scattering of solar Lyman- α photons, he showed that both maxima are related to the effect of solar radiation pressure. He argued that the presence of two maxima contradicts the notion that solar radiation pressure simply turns the line of apsides of satellite H orbits such that the apogees are pushed tailward.

[11] Using the Geocoronal Imager (GEO) on board the Imager for Magnetopause-to-Aurora Global Exploration (IMAGE) mission, Østgaard et al. [2003] derived H density profiles that were close to what was reported by Rairden et al. [1986]. However, above $8 R_E$, they found higher densities. They also confirmed the existence of a geotail and attributed this feature to solar Lyman- α radiation pressure on the satellite population.

[12] A group at the University of Bonn used Lyman- α measurements [Zoennchen et al., 2010] by Lyman- α detectors (LADs) on the Two Wide-angle Imaging Neutral-atom Spectrometers (TWINS) mission [McComas et al., 2009] to derive asymmetric exospheric H distributions for the Northern Hemisphere. They applied a conveniently simplified version [Nass et al., 2006] of the mathematical expansion developed by Hodges [1994] to obtain distributions in the summer months of 2008. As compared to Hodges [1994] and Østgaard et al. [2003], the Bonn group found significantly higher day-night asymmetry, showing a much more pronounced geotail. Additionally, the Bonn group observed much weaker pole-equator asymmetry than Hodges [1994].

[13] Prior models of exospheric H distributions were usually developed under assumptions of being spherically symmetric, or representative of typical (not actual) solar conditions, or averaged over an extended period of time. For example, the Chamberlain [1963] model is spherically symmetric and based entirely on theoretical predictions. The Rairden et al. [1986] model is spherically symmetric and it averages DE 1 observations over a 5 year period. While the Hodges [1994] model is asymmetric, its distributions were computationally rather than experimentally derived and are representative of typical solar cycle conditions at equinox and solstice. The Østgaard et al. [2003] model is asymmetric, but due to the specifics of GEO/IMAGE observational geometry it averages measurements over the time scale of a year.

[14] In this work, we use data obtained by LAD/TWINS, as does the Bonn group [Nass et al., 2006; Zoennchen et al., 2010]. We have expanded the Bonn model developed by Nass et al. [2006] to describe the distribution of exospheric H density. Specifically, our modifications include (1) additional fitting parameters sensitive to possible dawn-dusk asymmetry, (2) an accurate anisotropic photon scattering function, (3) a photon scattering rate at 1 AU (g-factor) obtained from independent measurements of the solar Lyman- α , and (4) an experimentally determined interplanetary glow background derived directly from Solar Wind Anisotropies (SWAN) measurements on the Solar and Heliospheric Observatory (SOHO) mission.

[15] Below, we describe the methodology by obtaining a global exospheric H density distribution on 11 June 2008, as an example. Depending on the observational coverage

available, we can apply this technique to other days. TWINS LAD data thus open a way to study how the asymmetric exosphere responds to varying seasons, solar conditions, and geomagnetic activity at certain time periods when data are available.

2. TWINS Lyman- α Experiment

2.1. Instrumentation

[16] The TWINS mission [McComas *et al.*, 2009] consists of two instruments, TWINS-1 and TWINS-2, on two separate satellites launched in 2006 and 2008 to stereoscopically image the magnetosphere in ENA fluxes, which are produced in charge exchange between magnetospheric energetic ions and exospheric background H atoms. To derive ion distributions from ENA measurements, knowledge of the exospheric H density distribution is necessary. Consequently, in addition to ENA imagers, each TWINS instrument includes a pair of identical Lyman- α detectors, LADs, to register line-of-sight (LOS) resonance scattered intensities. LAD data became available since June 2008.

[17] In each LAD, the incident radiation passes through a collimator followed by an optical interference filter centered at the wavelength 122 nm with a bandwidth 10 nm [Nass *et al.*, 2006]. The Lyman- α photons are then counted by a channel electron multiplier. The recorded photon count rate is proportional to the Lyman- α intensity and the geometric factor. The collimator on each LAD defines an aperture angle of 4° full width at half maximum. The sensor sensitivity is approximately $(2 \text{ cts s}^{-1})/R$, where $1 R = 1 \text{ rayleigh} = 10^6/(4\pi) \text{ phot cm}^{-2} \text{ s}^{-1} \text{ sr}^{-1}$. All LADs were calibrated, before the mission start, at the BESSY Synchrotron in Berlin [Richter *et al.*, 2001]. Typical intensities measured by the LADs are from 1000 to 10,000 R, with corresponding count rates from 2000 to 20,000 s^{-1} .

2.2. Observational Coverage

[18] The TWINS instruments fly on two satellites in widely spaced highly elliptical Molniya-type orbits, providing observational coverage from very different vantage points. On each satellite, two LADs, LAD-1 and LAD-2, observe the geocorona for several hours per orbit, where the orbital period is one half of a sidereal day. The TWINS instrument is located on a platform that rotates about a nominally nadir-pointed axis, in a windshield wiper motion, back and forth through overlapping angular limits $\Delta\omega = \pm 99^\circ$ with a rotational rate of approximately 3° per second (Figure 1). Thus, it takes approximately 1 min for LAD-1 and LAD-2, oriented 40° with respect to the actuator rotation axis, to observe a full circle around the Earth. LAD count rates are recorded every 0.67 and 1.33 s, corresponding to $\Delta\omega = 2^\circ$ and 4° of platform rotation. When the platform reaches $\omega = \pm 90^\circ$, LAD-1 will point in the same direction as LAD-2 in the opposite orientation, and vice versa, allowing for cross calibration of the sensors. In general, this observational geometry provides excellent coverage of the Northern Hemisphere, where the orbit apogees are located, but may be limited in the Southern Hemisphere.

[19] In total, we check 26 observational geometry and housekeeping limits before an LAD measurement is classified as valid for scientific analysis. To avoid the hazardous environment in the Van Allen radiation belts, all instruments

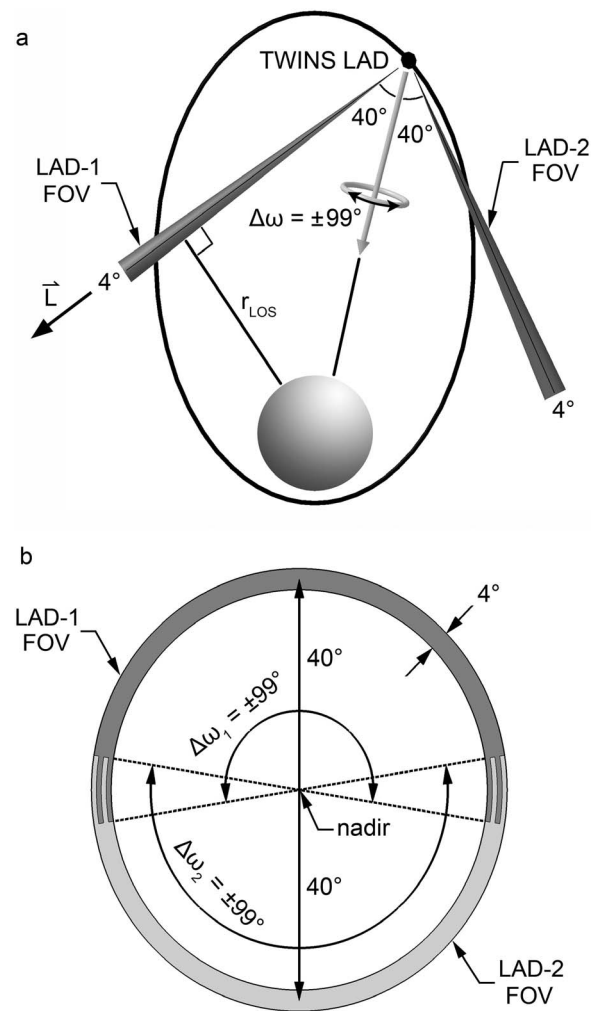


Figure 1. (a) Observational geometry of Lyman- α detectors (LAD-1 and LAD-2) on a Two Wide-angle Imaging Neutral-atom Spectrometers (TWINS) satellite in a highly elliptical Molniya-type orbit. The TWINS mission consists of two satellites, flying in similar orbits that are widely spaced. Both orbits have an apogee of $7.2 R_E$ over the Northern Hemisphere, an inclination of 63.4° , and an orbital period close to half a day. Variable r_{LOS} is the geocentric distance of an LAD line of sight, \mathbf{L} , with the closest approach to the Earth. Each LAD has a 4° full width half maximum field of view, pointed at 40° with respect to the rotating nominally nadir-pointed instrument platform axis. (b) LAD field of view coverage through the windshield wiper motion of the instrument platform. The light and dark shaded sections of the circle show the overlapping directions covered by LAD-1 (ω_1) and LAD-2 (ω_2), respectively, as the actuator rotates through the full motion ($\Delta\omega = \pm 99^\circ$). Note that detector measurements are only available within the limits $\Delta\omega = \pm 90^\circ$. The windshield wiper motion of the instrument platform results in the LAD fields of view covering a complete circle, centered on the Earth.

are turned off below an orbital radius of approximately $4.5 R_E$. During the orbit, the instrument rotation axis may drift away from nadir. Consequently, the geocentric distance of an LAD line of sight closest approach to the Earth, r_{LOS} ,

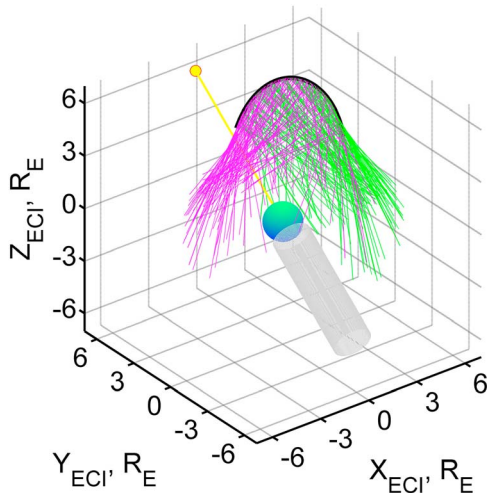


Figure 2. LAD observational coverage for TWINS-1 on 11 June 2008. The coordinate system is Earth centered inertial: the x axis points toward the vernal equinox, and the z axis is the celestial pole. The blue sphere is the Earth, the yellow line and dot show the direction to the Sun, the shaded cylinder is Earth's shadow, the black curve is the spacecraft trajectory, and the green and pink lines represent the line-of-sight vectors for LAD-1 and LAD-2, respectively.

varies from around 2.0 – $6.5 R_E$. Below $3 R_E$, the geocorona deviates substantially from being optically thin. Thus, those measurements with $r_{\text{LOS}} < 3 R_E$ are excluded. To mitigate possible solar contamination [Zoenchen *et al.*, 2010], only those measurements with a detector line of sight pointed at $>90^\circ$ from the direction to the Sun are used.

[20] Additionally, we require that the line of sight does not pass through Earth's shadow, approximated by a cylinder (with $1 R_E$ radius) in the antisolar direction. We note that crossing Earth's shadow opens a way of studying local number densities in this region by comparing the detector signal with adjacent fully illuminated lines of sight; such studies are beyond the scope of this work.

[21] Consider one TWINS satellite in an orbit with typical conditions. The pair of LADs records around $2 \times 8000 = 16,000$ valid measurements during the orbit. Adequate observational coverage around the Earth is essential to obtaining exospheric H distributions because a global fitting is only sensitive to the observed regions. For this study, we chose LAD data obtained on 11 June 2008 as the observational coverage for TWINS-1, shown in Figure 2, was excellent.

3. Model

[22] A process of modeling starts with an analytical expression for the three-dimensional H number density distribution. This expression contains free parameters that are best fit to the LAD observational data using a least squares curve fitting.

3.1. Coordinate System

[23] We use a geocentric coordinate system to describe exospheric H distributions, with the x axis pointed toward the intersection of the equator and noon meridian (equatorial noon) and z axis pointed to the celestial pole; the y axis

completes the orthogonal triad. The longitudinal angle ϕ is measured from the x axis in the XY plane and the colatitude angle θ is counted from the z axis, such that $\phi = 0^\circ$ and $\theta = 90^\circ$ points toward equatorial noon.

3.2. Spherical Harmonic Expansion

[24] Hodges [1994] modeled exospheric H number density distributions, $n_H(r, \phi, \theta)$, by a third-order spherical harmonic expansion in the form

$$n_H(r, \phi, \theta) = N(r) \sqrt{4\pi} \sum_{l=0}^3 \sum_{m=0}^l (A_{lm}(r) \cos(m\phi) + B_{lm}(r) \sin(m\phi)) Y_{lm}(\theta), \quad (1)$$

where $N(r)$ is the radial function, $A_{lm}(r)$ and $B_{lm}(r)$ are the radius-dependent coefficients of the expansion, and $Y_{lm}(\theta)$ are the spherical harmonic Legendre functions. He divided the geocentric distance r into 40 steps, which resulted in a total of 640 free parameters. Considering only the observational geometry limit with $r_{\text{LOS}} > 3 R_E$ reduces the number of free parameters to 96. This number of free parameters is still computationally impractical for a curve fitting procedure. Nass *et al.* [2006] suggested important simplifications, the Bonn model, that reduced the number of free parameters to 12. First, they reduced the order of the expansion, l , from 3 to 2. Second, they approximated the mean density, $N(r)$, by a power law

$$N(r) = pr^{-k}. \quad (2)$$

[25] Finally, for $A_{lm}(r)$, a linear approximation was used:

$$A_{lm}(r) = a_{lm} + b_{lm}r, \quad (3)$$

All $B_{lm}(r)$ were set to zero. Computer simulations [Nass *et al.*, 2006] showed that the Bonn model was able to conveniently reproduce major features of the Hodges [1994] model.

[26] We expanded the Bonn model in an important way by adding $B_{lm}(r)$ as free parameters, using a linear approximation:

$$B_{lm}(r) = c_{lm} + d_{lm}r, \quad (4)$$

which would open the opportunity to account for dawn-dusk asymmetry in the distribution, impossible if $B_{lm}(r) = 0$. This addition increases the number of free parameters in our model to 18, compared to 12 in the Bonn model.

4. Exospheric H Distribution

[27] The predicted intensity flux, F_P , as observed by the LADs in units of rayleigh (R), is

$$F_P = \frac{g^*}{10^6} \int_0^{L_{\text{max}}} n(\mathbf{L}) I(\alpha) dL + F_{\text{IP}}, \quad (5)$$

where $n(\mathbf{L})$ is the local H number density along the line of sight \mathbf{L} , $I(\alpha)$ is a factor that accounts for the angular dependence of scattered Lyman- α photons (see section 4.3), g^* is the local (adjusted to the actual heliocentric distance) g -factor, and F_{IP} is the interplanetary glow in rayleighs. The intensity of the geocorona decreases with increasing geo-

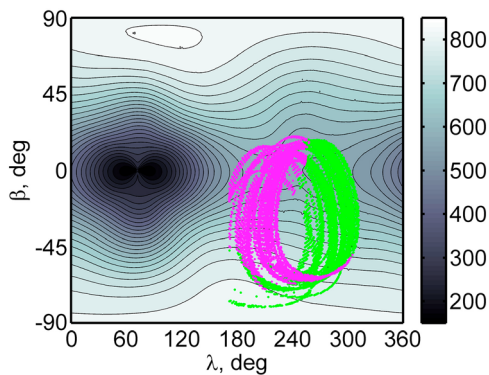


Figure 3. Interplanetary glow on 11 June 2008, derived from Solar Wind Anisotropies measurements (W. Pryor and R. Gladstone, personal communication, 2010). Green and pink dots are line-of-sight vectors for LAD-1 and LAD-2, respectively. The horizontal axis is ecliptic longitude λ , the vertical axis is ecliptic latitude β , and the color bar is in rayleighs.

centric distance. In our least squares curve fitting procedure, we integrate along the line of sight up to an L_{\max} of $50 R_E$ to ensure that all contributing regions of the geocorona are included.

4.1. Solar Output

[28] The local photon scattering rate, g^* , is determined by the spectral density at the center of the solar Lyman- α line profile. This spectral density, in turn, correlates with the total solar Lyman- α line flux [e.g., *Emerich et al.*, 2005]. The solar Lyman- α flux prominently varies over two time scales. First, the passage of active regions across the solar disk during a solar rotation period produces irradiance variations over approximately 27 days. Second, the solar activity cycle generates irradiance variations over approximately 11 years.

[29] For our model, we use solar Lyman- α measurements obtained from the Solar EUV Experiment (SEE) on the Thermosphere Mesosphere Energetic and Dynamics (TIMED) mission. During normal operations, SEE observes the Sun for about 3 min every orbit (orbital period ~ 97 min), providing 14 to 15 measurements per day (data available at the SEE/TIMED Web site, <http://lasp.colorado.edu/see/>, provided by the Laboratory for Atmospheric and Space Physics). On 11 June 2008, the average solar Lyman- α flux at 1 AU was 3.46×10^{11} photons $s^{-1} cm^{-2}$, which corresponds to a g-factor of $1.56 \times 10^{-3} s^{-1}$. The actual SEE/TIMED measurements varied within $\pm 5\%$ of the daily average.

4.2. Albedo From the Lower Geocorona

[30] The transition from the optically thick to optically thin regime in the exosphere is gradual with increasing geocentric distance. The brightness of the underlying optically thick region could be as high as 35 kR and its emission would constitute [*Østgaard et al.*, 2003; *Zoenchen et al.*, 2010], at distances $> 3 R_E$, less than 2% of the incident solar Lyman- α radiation. The exospheric emissions are confined however to a significantly narrower spectral band than the rather broad solar line. Detailed simulations by

Bishop [1999] show that the altitude-dependent contribution to the glow source function by the multiply scattered photons would vary, depending on the Sun angle, between 10%–20% and 5%–7% at geocentric distances $3 R_E$ and $8 R_E$, respectively. Consequently, the uncertainties of exospheric number densities obtained by us would also be of the same order, that is less than 20% at $3 R_E$ and decreasing with increasing geocentric distance.

4.3. Photon Scattering by H Atoms

[31] Hydrogen atoms scatter Lyman- α radiation anisotropically. The angular dependence of the scattered intensity, $I(\alpha)$, obtained by *Brandt and Chamberlain* [1959] is

$$I(\alpha) = 1 + \frac{1}{4} \left(\frac{2}{3} - \sin^2 \alpha \right). \quad (6)$$

For forward ($\alpha = 0^\circ$) and backward (180°) scattering, the probability deviates from the isotropic case by over 15%.

4.4. Interplanetary Glow

[32] The Sun resides inside a warm, partially ionized, low-density cloud of interstellar gas. Interstellar H atoms flow into the solar system filling interplanetary space [*Fahr*, 1974; *Holzer*, 1977; *Meier*, 1977; *Thomas*, 1978; *Bertaux*, 1984]. Similar to terrestrial H atoms, interplanetary atoms also resonantly scatter solar Lyman- α photons, producing the interplanetary glow. The SWAN instrument [*Bertaux et al.*, 1995] on SOHO made extensive observations of the interplanetary glow. The typical intensity of the interplanetary glow varies from 200 to 1000 R, depending on look direction and solar conditions.

[33] The LAD measured intensity is the sum of the geocoronal and interplanetary glow. From each LAD measurement, we subtract the interplanetary glow using an all-sky map (Figure 3) that was derived from SWAN measurements on 11 June 2008 (W. Pryor and R. Gladstone, personal communication, 2010). For all line-of-sight directions covered by the LADs on 11 June 2008, the interplanetary glow varied between 560 and 820 R, accounting for 10%–45% of the LAD measured intensities.

4.5. Fitting Procedure

[34] First, the simple r -dependent spherically symmetric density profile, $N(r) = pr^{-k}$, is fit, using the method of nonlinear least squares, with the 16 angular coefficients (a_{lm} , b_{lm} , c_{lm} , d_{lm}) set to zero. Second, once p and k have been obtained, their values are set and another fit is performed to obtain the angular coefficients. The fitting procedure is split into two steps because the parameter p must be varied over a much larger range than the others.

[35] Next, a new fit for p and k is conducted using the first pass values for the angular dependence coefficients. The new values for p and k are then used in another fit for a_{lm} , b_{lm} , c_{lm} , and d_{lm} , completing the second pass. The process was tested in an iterative fashion and one pass is usually sufficient to obtain the coefficients with accuracies better than 1%. A successful fit predicts the measured intensities to within a standard deviation of around 125 R, which would be, for example, less than 5% and 10% of typical intensities at distances $< 4 R_E$ and $< 6 R_E$, respectively. The random

Table 1. Parameters of the Exospheric H Number Density Distribution (Equations (1)–(4)) Obtained Using LAD Data From TWINS-1 on 11 June 2008^a

		Values
<i>Radial Parameters</i>		
p		4.1118×10^{13}
k		-2.5446
<i>Angular Parameters</i>		
a_{10}		-4.8992×10^{-2}
b_{10}		-1.8720×10^{-6}
a_{11}		-3.8248×10^{-1}
b_{11}		9.0636×10^{-6}
c_{11}		-4.8547×10^{-2}
d_{11}		-2.1587×10^{-6}
a_{20}		1.5739×10^{-1}
b_{20}		-6.1959×10^{-6}
a_{21}		-6.9198×10^{-2}
b_{21}		4.5477×10^{-6}
c_{21}		2.1922×10^{-1}
d_{21}		-7.0881×10^{-6}
a_{22}		-1.0148×10^{-1}
b_{22}		1.4873×10^{-6}
c_{22}		-8.8242×10^{-2}
d_{22}		4.2384×10^{-6}

^aVariable n_H is in cm^{-3} , and r is in km.

Poissonian error for the range of measured detector counts does not exceed 2%. The estimated uncertainty [e.g., *Bevington and Robinson, 2003*] in the obtained H density distribution slowly increases from 7% to 9% from $3 R_E$ to $6 R_E$ and then rapidly increases up to 25% at $8 R_E$.

[36] Using LAD data from TWINS-1 on 11 June 2008, a three-dimensional exospheric H number density distribution was obtained. The corresponding parameter values in equations (1)–(4) are listed in Table 1, where n_H is in cm^{-3} and r is in km.

4.6. Three-Dimensional Density Distribution

[37] Figure 4 shows cross sections of the three-dimensional exospheric H number density distribution obtained from TWINS-1 LAD data on 11 June 2008. The left panel shows a contour plot in the equatorial plane; day-night and dawn-dusk asymmetries are clearly visible. The right panel shows a contour plot in the meridional Earth-Sun plane, where one can see day-night and north-south asymmetries. We note that at larger geocentric distances, the inferring of density values becomes more challenging as the geocentric distance of an LAD line of sight closest approach to the Earth, r_{LOS} , where densities are highest, never exceeds $6.5 R_E$.

[38] The global distribution exhibits asymmetry in the day-night, dawn-dusk, and north-south directions. Figure 5 presents the angular variation of the distribution at geocentric distances $3 R_E$, $6 R_E$, and $8 R_E$. Similar to Figure 4, the left plots show number densities in the equatorial plane and the right plots in the meridional Earth-Sun plane.

[39] For lower geocentric distances, the dayside has noticeably higher densities than the nightside. This dayside maximum can be seen at $3 R_E$ (Figure 5, top) with $\phi \approx 60^\circ$ and $\theta \approx 155^\circ$. A nightside enhancement appears at $6 R_E$ (Figure 5, middle) with $\phi \approx 235^\circ$ and $\theta \approx 280^\circ$. At $8 R_E$ (Figure 5, bottom), this nightside enhancement becomes almost as pronounced as the dayside maximum. As the geocentric distance increases beyond $8 R_E$, the nightside densities become increasingly more pronounced than the dayside densities, consistent with the location of a geotail.

[40] The duskside has noticeably higher densities than the dawnside. This asymmetry can be seen in the left plots of Figure 5 as, compared to the dawnside with ϕ between 180° and 360° , generally higher densities exist on the duskside with ϕ between 0° and 180° .

[41] The right plots of Figure 5 clearly show that the Southern Hemisphere has noticeably higher densities than

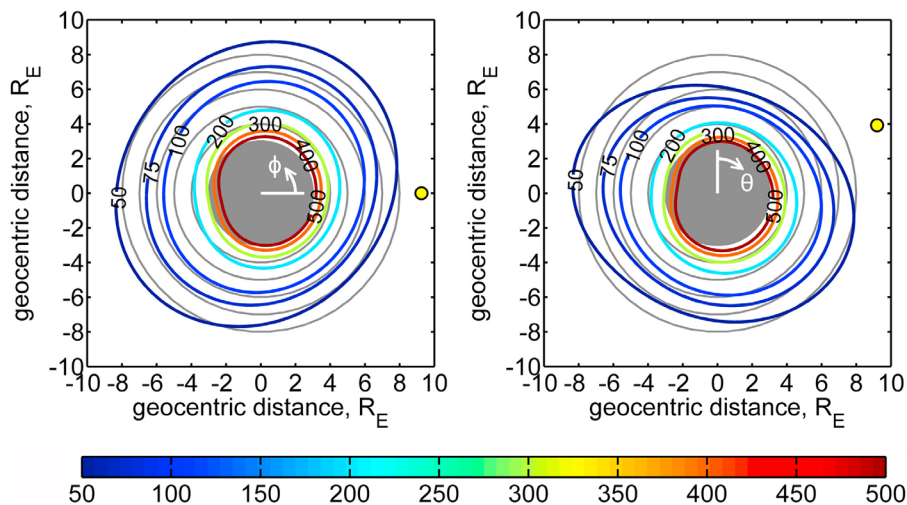


Figure 4. Contour plots of the exospheric H number density distribution on 11 June 2008: (left) an equatorial (xy plane) cross section and (right) a meridional (xz plane) cross section. Also shown are the definitions of the angles ϕ and θ . Contours are lines of constant neutral hydrogen number density (cm^{-3}); the color bar is for the contour lines; the yellow dot is the projection of the direction to the Sun (Figure 4, left) and the direction to the Sun (Figure 4, right); the filled shaded circle represents the region with radius $3 R_E$; and the grid of shaded concentric circles for $r > 3 R_E$, with a $1 R_E$ step, highlights the asymmetry of the distribution.

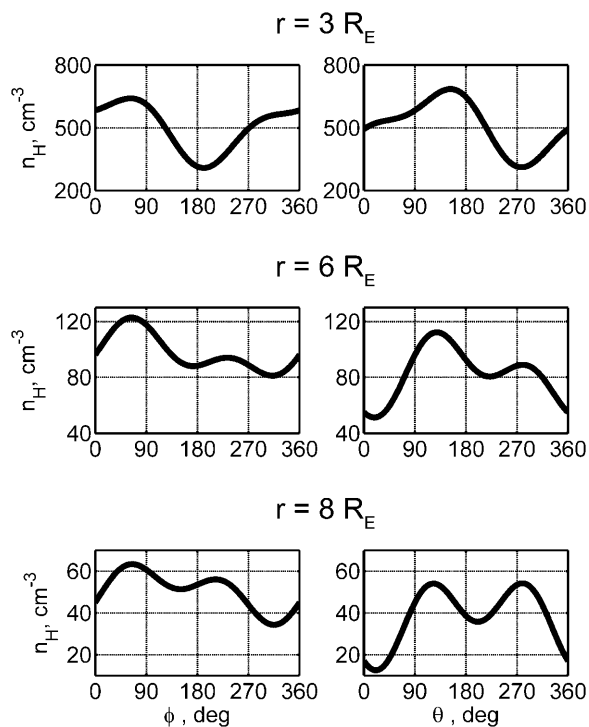


Figure 5. Exospheric H number density as a function of angles ϕ and θ for geocentric distances (top) $3 R_E$, (middle) $6 R_E$, and (bottom) $8 R_E$. In Figure 5 (left), ($\theta = 90^\circ$), angle $\phi = 0^\circ$ is equatorial noon and $\phi = 90^\circ$ is dusk. In Figure 5 (right), ($\phi = 0^\circ$), angle $\theta = 0^\circ$ is north and $\theta = 90^\circ$ is equatorial noon.

the Northern Hemisphere. This observed asymmetry is consistent with the Hodges [1994] solstice distributions.

[42] We note that the coverage of the exosphere by LAD observations is incomplete, as determined by the mission geometry. The obtained asymmetry of the H distribution should be more sensitive to the incomplete coverage than the averaged radial density profile $N(r)$. We plan to investigate in the future possible effects of incomplete coverage.

5. Discussion

5.1. H Density Radial Profile

[43] Figure 6 compares the spherically symmetric radial component, $N(r)$, of our exospheric H distribution to prior models. Our density profile is remarkably close to those obtained by Rairden *et al.* [1986], Hodges [1994], and Østgaard *et al.* [2003], with differences less than 50% between $3 R_E$ and $8 R_E$.

[44] The conditions of our observation on 11 June 2008 correspond to solar minimum. The DE 1 measurements used by Rairden *et al.* [1986] were obtained over a different phase of the solar cycle, during the solar activity increase from 1981 to 1985. Østgaard *et al.* [2003] also reported on a different phase of the solar cycle as they used GEO/IMAGE measurements near solar maximum from June 2000 to June 2001. In addition to being solar minimum with an F10.7 value of 66, our observation was seasonally close to summer solstice. Thus, the Hodges [1994] solstice distribution with an F10.7 value of 80 represents the most similar conditions.

[45] For geocentric distances $r > 4.5 R_E$, the Zoenchen *et al.* [2010] density profile shows somewhat higher densities than those by Rairden *et al.* [1986], Hodges [1994], and Østgaard *et al.* [2003], as well as ours. The possible causes for this difference are currently being investigated.

5.2. H Distribution Asymmetry

[46] Similar to Hodges [1994], our distribution exhibits an enhancement in the antisolar direction (geotail) and an enhancement in the solar direction. Figure 7 shows the density distribution along four radial directions: north, south, equatorial noon, and equatorial midnight, from $3 R_E$ to $8 R_E$. While our model describes number densities at larger geocentric distances, validating the values beyond $8 R_E$ becomes increasingly difficult. However, we note that our densities are consistent with the H densities inferred from measurements by the Interstellar Boundary Explorer (IBEX) mission [Fuselier *et al.*, 2010], which carries sensitive ENA detectors. Fuselier *et al.* [2010] recently reported an H number density range of $4\text{--}11 \text{ cm}^{-3}$ at the subsolar magnetopause ($\sim 10 R_E$ geocentric distance along the Earth-Sun line).

[47] For geocentric distances $r < 6 R_E$, the density profile for equatorial noon is higher than for equatorial midnight. As the geocentric distance increases, the density profile for equatorial midnight decreases less rapidly than for equatorial noon until the former becomes dominant, similar to the asymmetry observed by Østgaard *et al.* [2003]. This asymmetry is less pronounced than that of Zoenchen *et al.* [2010].

[48] A north-south asymmetry also exists, such that the H densities are depleted at higher geocentric distances in the Northern Hemisphere. At $4 R_E$, the southern polar region has 40% higher densities than in the northern polar region;

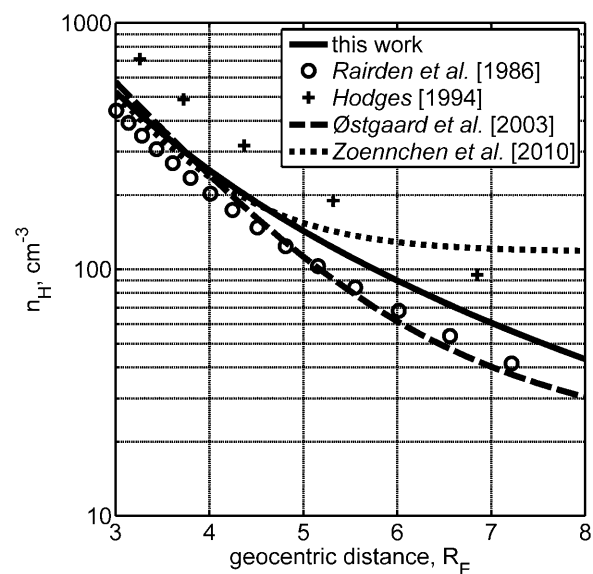


Figure 6. Comparison of different H number density profiles on 11 June 2008 from this work (solid line), Rairden *et al.* [1986] (circles), Hodges [1994] at solstice for F10.7 = 80 (crosses), Østgaard *et al.* [2003] for solar zenith angle 90° (long dashed line), and Zoenchen *et al.* [2010] on 11 June 2008 (short dashed line).

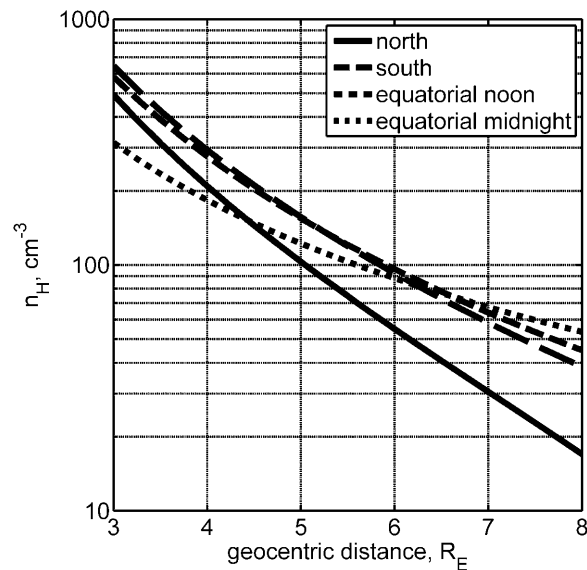


Figure 7. Exospheric H number density radial dependencies of the 11 June 2008 distribution from this work toward north (solid line), south (long dashed line), equatorial noon (short dashed line), and equatorial midnight (dotted line).

increasing to 70% at $6 R_E$ and 125% at $8 R_E$. This asymmetry is likely caused by the Sun's position near summer solstice at this time. The Hodges [1994] solstice distributions exhibit similar asymmetry. While his solstice distribution for F10.7 = 80 is nearly symmetric at lower geocentric distances, beyond $4 R_E$ densities in the Northern Hemisphere decrease more rapidly than in the Southern Hemisphere.

5.3. H Densities at Larger Geocentric Distances

[49] In addition to the propagated fitting error (section 4.5), the obtained exospheric H number density distribution uncertainty increases for larger geocentric distances as the intensity of the geocorona is exceeded by that of the interplanetary glow. To illustrate the effect of this uncertainty, the radial dependence of predicted intensity on the position of a hypothetical observer looking radially away from the Earth is plotted in Figure 8.

[50] For the TWINS-1 LAD observational geometry on 11 June 2008, the interplanetary glow intensity varied from 560 to 820 R. Thus, for geocentric distances $r > 8 R_E$, the interplanetary glow becomes comparable or dominates the observed intensities. Consequently, intrinsic uncertainty in the interplanetary glow map, which is difficult to precisely quantify as the map is obtained by complex reduction of SWAN/SOHO observations, could make the predictions of exospheric H distributions at large distances less reliable. Also, the use of accurate anisotropic scattering of Lyman- α photons [Brandt and Chamberlain, 1959], which deviates up to 15% from the isotropic case, is essential to avoid artifacts in reconstructed distributions.

6. Conclusions

[51] LAD measurements from TWINS-1 on 11 June 2008 have been used to obtain a global exospheric H distribution

for geocentric distances from $3 R_E$ to $8 R_E$. For larger distances, uncertainty in the derived distribution accuracy increases for two reasons. First, the observational geometry is limited by a geocentric distance for an LAD line-of-sight closest approach to the Earth, r_{LOS} , that does not exceed $6 R_E$. Second, accurate knowledge of the interplanetary glow becomes increasingly important as, above $8 R_E$, it dominates the observed intensities.

[52] The radial dependence of our spherically symmetric distribution is in agreement with the density profiles obtained by Rairden *et al.* [1986], Hodges [1994], and Østgaard *et al.* [2003]. For geocentric distances $r > 4.5 R_E$, their density profiles, as well as ours, decrease more rapidly than that obtained by Zoennchen *et al.* [2010].

[53] In our global distribution, we confirm the existence of an H density enhancement on the dayside, a feature previously reported by Tinsley *et al.* [1986] and Hodges [1994]. Our distribution also exhibits an enhancement on the nightside, consistent with the location of a geotail, in agreement with the day-night asymmetry described by Østgaard *et al.* [2003], but less pronounced than reported by Zoennchen *et al.* [2010]. Another prominent asymmetry exists in the north-south direction, with larger densities in the Southern Hemisphere, similar to the Hodges [1994] solstice distributions for similar seasonal conditions. The dawn-dusk asymmetry is less prominent, but visible with densities slightly higher on the duskside. These asymmetries may be of particular interest to magnetospheric ENA imaging, which heretofore has largely relied on the spherically symmetric distribution of Rairden *et al.* [1986].

[54] The obtained distribution demonstrates that TWINS LAD data are sensitive to asymmetry of the exosphere. Such distributions can be obtained, in principle, on a daily basis when TWINS has adequate coverage of the near-Earth region. Consequently, the results of this work lay the foundation for

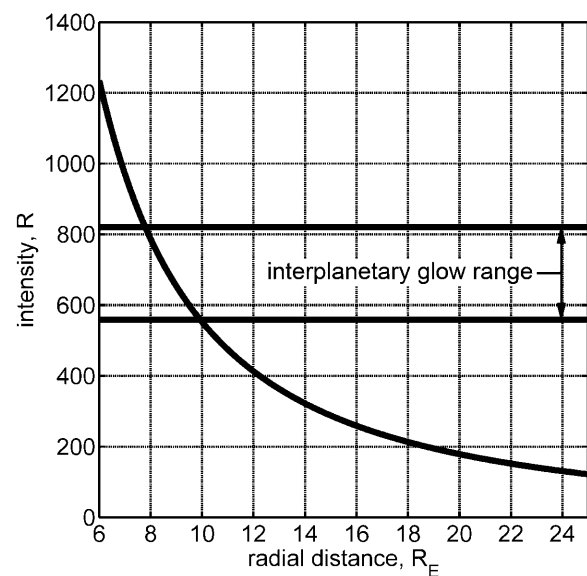


Figure 8. The radial dependence of predicted intensity on the position of a hypothetical observer looking radially away from the Earth. Two horizontal lines show the range of interplanetary glow intensities for all directions covered by the LADs on 11 June 2008.

study of the dynamic exosphere, responding to varying solar conditions and geomagnetic activity, as described by commonly used indices. Furthermore, seasonal variations, particularly at equinox and solstice, can be examined.

[55] **Acknowledgments.** The authors gratefully thank the TWINS team (PI Dave McComas) for making this work possible. We especially thank Hans Fahr, Uwe Nass, Jochen Zoennchen, and the late Guenter Lay for discussions; W. Kent Tobiska for support with solar irradiance data; and Wayne Pryor and Randy Gladstone for providing the interplanetary glow map. We thank two reviewers for helpful comments and suggestions. This work is supported in part by the NASA TWINS mission. J.B. acknowledges support by a Northrop Grumman fellowship.

[56] Robert Lysak thanks the reviewers for their assistance in evaluating this paper.

References

- Anderson, D. E., Jr., and C. W. Hord (1977), Multidimensional radiative transfer: Applications to planetary coronae, *Planet. Space Sci.*, *25*, 563–571, doi:10.1016/0032-0633(77)90063-0.
- Bertaux, J. L. (1984), Helium and hydrogen of the local interstellar medium observed in the vicinity of the Sun, *NASA Conf. Publ.*, CP 2345, 3–23.
- Bertaux, J. L., and J. E. Blamont (1970), OGO-5 measurements of Lyman- α intensity distribution and linewidth up to 6 Earth radii, *Space Res.*, *10*, 591–601.
- Bertaux, J. L., and J. E. Blamont (1973), Interpretation of OGO 5 Lyman alpha measurements in the upper geocorona, *J. Geophys. Res.*, *78*, 80–91, doi:10.1029/JA078i001p00080.
- Bertaux, J. L., et al. (1995), SWAN: A study of solar wind anisotropies on SOHO with Lyman alpha sky mapping, *Sol. Phys.*, *162*, 403–439, doi:10.1007/BF00733435.
- Bevington, P. R., and D. K. Robinson (2003), Error analysis, in *Data Reduction and Error Analysis for the Physical Sciences*, pp. 36–50, McGraw-Hill, New York.
- Bishop, J. (1985), Geocoronal structure: The effects of solar radiation pressure and the plasmasphere interaction, *J. Geophys. Res.*, *90*, 5235–5245, doi:10.1029/JA090iA06p05235.
- Bishop, J. (1999), Transport of resonant atomic hydrogen emissions in the thermosphere and geocorona: Model description and applications, *J. Quant. Spectrosc. Radiat. Transf.*, *61*(4), 473–491, doi:10.1016/S0022-4073(98)00031-4.
- Brandt, J. C., and J. W. Chamberlain (1959), Hydrogen radiation in the night sky, *Astrophys. J.*, *130*, 670–682, doi:10.1086/146756.
- Bush, B. C., and S. Chakrabarti (1995), Analysis of Lyman α and He I 584-Å airglow measurements using a spherical radiative transfer model, *J. Geophys. Res.*, *100*, 19,609–19,625, doi:10.1029/95JA01210.
- Carruthers, G. R., T. Page, and R. R. Meier (1976), Apollo 16 Lyman alpha imagery of the hydrogen geocorona, *J. Geophys. Res.*, *81*, 1664–1672, doi:10.1029/JA081i010p01664.
- Chamberlain, J. W. (1963), Planetary coronae and atmospheric evaporation, *Planet. Space Sci.*, *11*, 901–960, doi:10.1016/0032-0633(63)90122-3.
- Chamberlain, J. W. (1979), Depletion of satellite atoms in a collisionless exosphere by radiation pressure, *Icarus*, *39*, 286–294, doi:10.1016/0019-1035(79)90171-4.
- Clarke, J. T., R. Lallement, J. L. Bertaux, H. Fahr, E. Quémerais, and H. Scherer (1998), HST/GHRS observations of the velocity structure of interplanetary hydrogen, *Astrophys. J.*, *499*, 482–488, doi:10.1086/305628.
- Donahue, T. M. (1966), The problem of atomic hydrogen, *Ann. Geophys.*, *22*, 175–188.
- Emerich, C., P. Lemaire, J. Vial, W. Curdt, U. Schühle, and K. Wilhelm (2005), A new relation between the central spectral solar H I Lyman α irradiance and the line irradiance measured by SUMER/SOHO during the cycle 23, *Icarus*, *178*, 429–433, doi:10.1016/j.icarus.2005.05.002.
- Fahr, H. J. (1974), The extraterrestrial UV-background and the nearby interstellar medium, *Space Sci. Rev.*, *15*, 483–540, doi:10.1007/BF00178217.
- Fuselier, S. A., et al. (2010), Energetic neutral atoms from the Earth's subsolar magnetopause, *Geophys. Res. Lett.*, *37*, L13101, doi:10.1029/2010GL044140.
- Gruntman, M., and V. Izmodenov (2004), Mass transport in the heliosphere by energetic neutral atoms, *J. Geophys. Res.*, *109*, A12108, doi:10.1029/2004JA010727.
- Hodges, R. R. (1994), Monte Carlo simulation of the terrestrial hydrogen exosphere, *J. Geophys. Res.*, *99*, 23,229–23,247, doi:10.1029/94JA02183.
- Holzer, T. E. (1977), Neutral hydrogen in interplanetary space, *Rev. Geophys.*, *15*, 467–490, doi:10.1029/RG015i004p00467.
- Kupperian, J. E., Jr., E. T. Byram, T. A. Chubb, and H. Friedman (1959), Far ultraviolet radiation in the night sky, *Planet. Space Sci.*, *1*, 3–6, doi:10.1016/0032-0633(59)90015-7.
- Mange, P., and R. Meier (1970), OGO 3 observations of the Lyman alpha intensity and the hydrogen concentration beyond 5 Re, *J. Geophys. Res.*, *75*, 1837–1847, doi:10.1029/JA075i010p01837.
- McComas, D. J., et al. (2009), The Two Wide-angle Imaging Neutral-atom Spectrometers (TWINS) NASA mission-of-opportunity, *Space Sci. Rev.*, *142*, 157–231, doi:10.1007/s11214-008-9467-4.
- Meier, R. R. (1969), Balmer alpha and Lyman beta in the hydrogen geocorona, *J. Geophys. Res.*, *74*, 3561–3574, doi:10.1029/JA074i014p03561.
- Meier, R. R. (1977), Some optical and kinetic properties of the nearby interstellar gas, *Astron. Astrophys.*, *55*, 211–219.
- Meier, R. R., and P. Mange (1970), Geocoronal hydrogen: An analysis of the Ly- α airglow observed from OGO-4, *Planet. Space Sci.*, *18*, 803–821, doi:10.1016/0032-0633(70)90080-2.
- Meier, R. R., and P. Mange (1973), Spatial and temporal variations of the Lyman-alpha airglow and related atomic hydrogen distributions, *Planet. Space Sci.*, *21*, 309–327, doi:10.1016/0032-0633(73)90030-5.
- Nass, H. U., J. H. Zoennchen, G. Lay, and H. J. Fahr (2006), The TWINS-LAD mission: Observations of terrestrial Lyman- α fluxes, *Astrophys. Space Sci. Trans.*, *2*, 27–31, doi:10.5194/astra-2-27-2006.
- Østgaard, N., S. B. Mende, H. U. Frey, G. R. Gladstone, and H. Lauche (2003), Neutral hydrogen density profiles derived from geocoronal imaging, *J. Geophys. Res.*, *108*(A7), 1300, doi:10.1029/2002JA009749.
- Quémerais, E., J. L. Bertaux, R. Lallement, B. Sandel, and V. Izmodenov (2003), Voyager 1/UVS Lyman α glow data from 1993 to 2003: Hydrogen distribution in the upwind outer heliosphere, *J. Geophys. Res.*, *108*(A10), 8029, doi:10.1029/2003JA009871.
- Rairden, R. L., L. A. Frank, and J. D. Craven (1983), Geocoronal imaging with dynamics explorer: A first look, *Geophys. Res. Lett.*, *10*, 533–536, doi:10.1029/GL010i007p00533.
- Rairden, R. L., L. A. Frank, and J. D. Craven (1986), Geocoronal imaging with dynamics explorer, *J. Geophys. Res.*, *91*, 13,613–13,630, doi:10.1029/JA091iA12p13613.
- Richter, M., U. Kroth, R. Thomagel, H. J. Fahr, G. Lay, and H. U. Nass (2001), Calibration of Lyman- α detectors for the NASA satellites TWINS, *Annu. Rep. S15*, BESSY, Berlin.
- Schwadron, N. A., and D. J. McComas (2010), Pickup ions from energetic neutral atoms, *Astrophys. J.*, *712*, L157–L159, doi:10.1088/2041-8205/712/2/L157.
- Stephan, S. G., S. Chakrabarti, J. Vickers, T. Cook, and D. Cotton (2001), Interplanetary H Ly α observations from a sounding rocket, *Astrophys. J.*, *559*, 491–500, doi:10.1086/322322.
- Thomas, G. E. (1963), Lyman α scattering in the Earth's hydrogen geocorona, *J. Geophys. Res.*, *68*, 2639–2660, doi:10.1029/JZ068i009p02639.
- Thomas, G. E. (1970), Ultraviolet observations of atomic hydrogen and oxygen from the OGO satellites, *Space Res.*, *10*, 602–607.
- Thomas, G. E. (1978), The interstellar wind and its influence on the interplanetary environment, *Annu. Rev. Earth Planet. Sci.*, *6*, 173–204, doi:10.1146/annurev.ea.06.050178.001133.
- Thomas, G. E., and D. E. Anderson Jr. (1976), Global atomic hydrogen density derived from OGO-6 Lyman alpha measurements, *Planet. Space Sci.*, *24*, 303–312, doi:10.1016/0032-0633(76)90042-8.
- Thomas, G. E., and R. C. Bohlin (1972), Lyman-alpha measurements of neutral hydrogen in the outer geocorona and in interplanetary space, *J. Geophys. Res.*, *77*, 2752–2761, doi:10.1029/JA077i016p02752.
- Tinsley, B. A., R. R. Hodges, and R. P. Rohrbaugh (1986), Monte Carlo models for the terrestrial exosphere over a solar cycle, *J. Geophys. Res.*, *91*, 13,631–13,647, doi:10.1029/JA091iA12p13631.
- Wallace, L., C. A. Barth, J. B. Pearce, K. K. Kelly, D. E. Anderson Jr., and W. G. Fastie (1970), Mariner 5 measurement of the Earth's Lyman alpha emission, *J. Geophys. Res.*, *75*, 3769–3777, doi:10.1029/JA075i019p03769.
- Zoennchen, J. H., U. Nass, G. Lay, and H. J. Fahr (2010), 3-D-geocoronal hydrogen density derived from TWINS Ly- α -data, *Ann. Geophys.*, *28*, 1221–1228, doi:10.5194/angeo-28-1221-2010.

J. Bailey and M. Gruntman, Department of Astronautical Engineering, Viterbi School of Engineering, University of Southern California, Los Angeles, CA 90089-1192, USA. (jjbailey@usc.edu)